Impact of the Input Baseband Terminations on the Efficiency of Wideband Power Amplifiers Under Concurrent Band Operation

Diogo R. Barros, *Student Member, IEEE*, Luís C. Nunes, *Member, IEEE*, Pedro M. Cabral, *Senior Member, IEEE*, and José Carlos Pedro, *Fellow, IEEE*

***Abstract*— This article presents a theoretical explanation of the efficiency degradation in wideband radio frequency power amplifiers (RFPAs) under concurrent dual-band operation that is still visible after eliminating all known causes related to the output matching network (OMN). First, the origin of this degradation, identified by the reduction of the PA's efficiency and linearity, is traced to the input baseband impedance terminations. Then, a theoretical model that describes the phenomenon and qualitatively predicts the efficiency variation under concurrent dual-band operation is presented using a simple model based on two-tone excitation. Finally, the proposed explanation is confirmed by comparing the efficiency performance of two 30-W GaN RFPAs of distinct instantaneous bandwidth determined by different input video-bandwidth terminations, under two-tone and concurrent dual-band operation. This article shows that, in addition to the adequate OMN design, an optimal input baseband impedance profile is also an important design constraint needed to keep the efficiency and linearity performance of RFPAs, for scenarios that require a wide instantaneous bandwidth.**

***Index Terms*— Baseband impedance, instantaneous bandwidth, power amplifiers, video bandwidth, wideband.**

I. Introduction

BANDWIDTH and energy efficiency are two of the most important factors that shape the evolution of wireless communications systems. On the one hand, wide bandwidth is required to cope with the progressively higher data rate demand, as in wideband multicarrier/concurrent band scenarios. On the other hand, there is a widespread interest to minimize the energy consumption of these systems, not only for operational cost reduction but also for environmental awareness. Therefore, an extensive research effort is being made to fully understand the phenomena that leads to performance degradation when a power amplifier (PA) is no longer excited with a continuous wave (CW) signal but with one of considerable instantaneous bandwidth [1]–[3].

Several studies have shown that the baseband impedance terminations are an important cause of performance degradation, and therefore, methods to correct it have been proposed. Williams *et al.* [4] have shown how the output and input baseband terminations affect the IM3 distortion, through the envelope analysis of measured time-domain waveforms. Bunz *et al.* [5] have reported linearity and efficiency degradation from both the input and output baseband terminations through experimental envelope source and load–pull measurements. Hu *et al.* [6] showed that an appropriate injection of the second-order baseband intermodulation component at the input, through feedback, can reduce the third-order intermodulation distortion (IMD) by 12 dB. Kwon *et al.* [7] have reported that the fifth-order IMD could also be improved by optimal control of the amplitude and phase of the injected second-order baseband intermodulation product. Chaudhary [8] reported an impedance optimization scheme at higher order baseband components.

To allow optimal device performance for wideband applications, devices started to include in-package circuitry to provide wideband low baseband impedance terminations at the device's intrinsic terminals [9]. In addition, baseband characterization and measurement methods have also been improved [10], [11].

Recently, Nunes *et al.* [12] reported a theoretical study of the efficiency degradation induced by the output baseband impedance terminations. However, the input baseband impedance impact on the wideband PA's efficiency is still largely unexplored and commonly ignored during the design stage. Only more recently, the mechanism of efficiency degradation associated with the input baseband impedance was introduced in [13], explaining that if it is not properly addressed, a bias fluctuation is generated, inducing a severe linearity and efficiency degradation in scenarios that require a very wide instantaneous bandwidth.

Therefore, the aim of this article is to expand the analysis presented in [13], explaining in a comprehensive, qualitative, and quantitative way, how the bias fluctuation generated by the baseband impedance terminations affects the PA performance

Manuscript received May 4, 2019; revised September 20, 2019; accepted October 28, 2019. Date of publication December 4, 2019; date of current version December 27, 2019. This work was supported in part by Fundação para a Ciência e a Tecnologia (FCT)/Ministério da Educação e Ciência (MEC) through national funds, in part by Fundo Europeu de Desenvolvimento Regional (FEDER)—PT2020 Partnership Agreement under Project PTDC/EEI-TEL/30534/2017, Project UID/EEA/50008/2019, and in part by Huawei Technologies Sweden AB. The work of D. R. Barros was supported by a Ph.D. under Grant SFRH/BD/148388/2019. This article is an expanded article from the IEEE MTT-S International Microwave Symposium held on June 2–7, 2019 in Boston, MA, USA. *(Corresponding author: Diogo R. Barros.)*

The authors are with Dep. de Eletrónica, Telecomunicações e Informática (DETI), Instituto de Telecomunicações, Universidade de Aveiro, 3810-193 Aveiro, Portugal (e-mail: diogo.rafael@ua.pt; cotimos@ua.pt; pcabral@ua.pt; jcpedro@ua.pt).

Color versions of one or more of the figures in this article are available online at http://ieeexplore.ieee.org.

Digital Object Identifier 10.1109/TMTT.2019.2951147

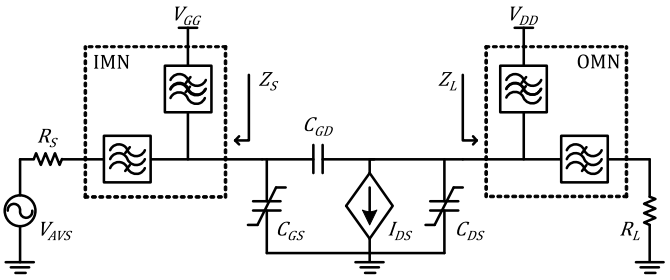

Fig. 1. Simplified circuit representation of an RFPA.

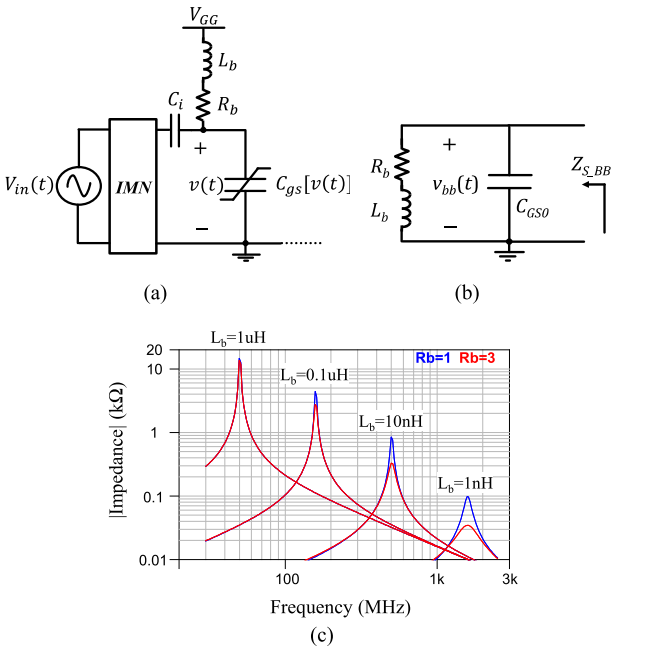

Fig. 2. (a) Conventional input bias circuit with stabilization resistor, (b) respective small-signal equivalent circuit, and (c) impedance profiles for several inductor and resistor values (with Cgs0 = 10 pF).

when excited with a wideband signal. For that, a simple model is advanced to estimate the efficiency degradation related to the input baseband impedance.

This article is structured as follows. First, in Section II, we revisited the performance degradation mechanisms due to the baseband impedance terminations. In Section III, we derive a simple theoretical model that is used to understand and to predict their impact on the PA's performance. Three specific baseband impedance termination scenarios were considered, which led to distinct degradation profiles. In Section IV, we experimentally demonstrate that the input baseband terminations can degrade PA performance and that it can be prevented through adequate IMN design. In addition, we demonstrate that the theoretical model is able to predict the performance degradation of practical wideband PAs, and thus, be used as a simple and fast tool to evaluate its instantaneous bandwidth. Finally, the conclusions of this article are summarized in Section V.

II. Efficiency Degradation Mechanism Related With the Input Baseband Termination

Let us consider the simplified circuit representation of a radio frequency PA (RFPA) presented in Fig. 1. The PA is composed by three main blocks: the output matching network (OMN) to provide the required power and efficiency impedance matching at the output; the input matching network (IMN) to impose the matching for gain and stable operation; and finally, the device itself, whose nonlinear internal capacitances are determinant for this analysis. Please note that, since the device's extrinsic components are linear, they can be integrated into the matching networks.

As shown in [5], the OMN needs to provide nearly ideal baseband termination conditions, i.e., very low impedance to the intrinsic drain of the device, to prevent the output dependent efficiency and linearity degradation under modulated signal excitation. We assume that the OMN is always optimized to present optimal baseband impedance terminations in practical PA design so that we can focus solely on the performance degradation due to the IMN's baseband profile.

The profile of the input baseband impedance, Z_{S_BB}, is commonly imposed by the input bias circuitry. As a result, Z_{S_BB} is connected in parallel with both the C_{GS} and the input Miller reflected C_{GD}. Since the output baseband impedance is assumed to be short circuit, the voltage gain at the baseband components is zero, and therefore, the Miller component is simply the C_{GS} value. From this point on, this C_{GD} Miller component is assumed to always be integrated into C_{GS} and will no longer be directly referred to in the remainder of this analysis.

In a conventional IMN design, a large inductor or a high characteristic impedance transmission line is commonly used in series with a resistor to simultaneously decouple the RF path from the bias circuit and ensure stable operation. This type of bias network is shown in Fig. 2(a). While this method greatly simplifies the design, Z_{S_BB} is commonly inductive in nature at low frequencies and, therefore, forms a parallel resonant circuit together with C_{GS}, as shown in Fig. 2(b). Depending on the quality factor, the baseband impedance at the resonant frequency can be very high, as presented in Fig. 2(c).

The reason why most PA designers ignore the input baseband impedance is that they assume that there is no current at the input of the device at these frequencies. However, these components are generated due to the nonlinearity introduced by the C_{GS} variation when the input is a wideband modulated signal. Since C_{GS} is a nonlinear capacitance, its current, i_C, is given by

$$i_C(t) = C_{GS}[v(t)]\frac{dv(t)}{dt} \tag{1}$$

where $C_{GS}[v(t)]$ describes the variation of the capacitance with the intrinsic gate voltage. For instance, if we approximate the $C_{GS}[v(t)]$ variation (normally modulated by a hyperbolic tangent function [14]) with a first-order polynomial function

$$C_{GS}(v(t)) = C_{gs0} + C_{gs1}v(t) \tag{2}$$

which corresponds to a quadratic charge function

$$Q_{GS}(v(t)) = q_{gs0} + C_{gs0}v(t) + \frac{C_{gs1}}{2}v(t)^2. \tag{3}$$

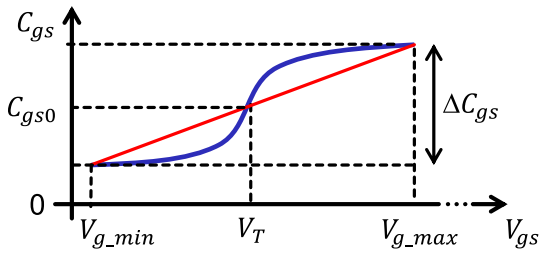

Fig. 3. $C_{\mathrm{GS}}[v(t)]$ nonlinear profile and the respective curve fitting with a first-order polynomial model.

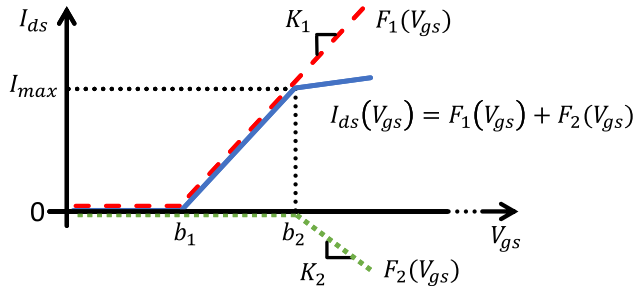

Fig. 4. Piecewise linear functions used to approximate the current source behavior: current mode operation (red dashed line), current saturation (blue solid line), and complete model (green dots).

Thus, the resulting baseband current component is

$$i_{\mathrm{BB}}(t) = -\frac{1}{4} V_P^2 C_{\mathrm{gs1}} \omega_m \sin(2\omega_m t) \tag{4}$$

where V_P is the peak excitation voltage, and ω_m is half of the separation frequency. The coefficients C_{gs0} and C_{gs1} can be extracted using least squares and assuming a sinusoidal input excitation with the maximum $v(t)$ voltage amplitude, as shown in Fig. 3.

Since this current is supplied by the bias network circuit presented in Fig. 2(b), the baseband voltage developed at the intrinsic gate is given by

$$v_{\mathrm{BB}}(t) = V_{\mathrm{GG}} + \frac{1}{4} |Z_{S_{\mathrm{BB}}}(2\omega_m)| V_P^2 C_{\mathrm{gs1}} \omega_m \sin[2\omega_m t + \angle(Z_{S_{\mathrm{BB}}}(2\omega_m))]. \tag{5}$$

Please note that, by considering that $C_{\mathrm{GS}}[v(t)]$ is only excited by the fundamental voltage component, we are neglecting the nonlinear feedback, i.e., the change in the fundamental voltage component due to the baseband component is not fed back into the model to update v_{BB}. However, even with this simplification, the model can predict reasonably well the bias fluctuation, as it will be shown later on.

For a typical inductive baseband impedance, $Z_{S\_\mathrm{BB}} = j\omega_m L$, v_{BB} rises with the square of ω_m. Therefore, a large v_{BB} fluctuation can be generated at the intrinsic gate node at $2\omega_m$, disturbing the normal quiescent point of the PA. In particular, the conduction angle of the PA is changed between classes-A and C within the period of the envelope, leading to a variation of its linearity and efficiency, as shown in Section III.

Please note that v_{BB} is proportional not only to the magnitude of Z_{S_BB}, but also to the amplitude and bandwidth of the input signal and the variation of C_{GS}. Therefore, wideband, high-power PAs, which normally present higher C_{GS} variation, are expected to be more susceptible to the described phenomena, for the same baseband impedance conditions.

III. Impact of Input Baseband Voltage Fluctuation

In Section II, we have observed that the nonlinear C_{GS} can create an intrinsic baseband voltage fluctuation, which depends on the amplitude and phase of baseband termination, Z_{S_BB}.

To analyze the impact of the v_{BB} fluctuation, we use a current source model based on the piecewise linear squashing technique, as was already proposed in [15] and [16] to be able to directly calculate the fundamental and baseband components of the PA current. The model is composed of two piecewise linear functions, F_n, with different gains/derivatives (K_n) and input bias (b_n), as shown in Fig. 4, in which F_1 describes the current mode operation, and F_2 imposes the current saturation profile typically observed in highly efficient overdriven PAs. With this, we preserve the simplicity of the model without losing the qualitative representation of the PA's normal operation.

As a consequence of the model's simplicity, we can analytically compute the dc and fundamental Fourier components of each function, according to

$$I_0(V_{\mathrm{GG}}, A) = \sum_{n=1}^{2} \frac{K_n}{\pi} [(V_{\mathrm{GG}} - b_n)\theta_n + A \sin(\theta_n)] \tag{6}$$

$$I_1(V_{\mathrm{GG}}, A) = \sum_{k=1}^{2} \frac{K_n A}{2\pi} [2\theta_n - \sin(2\theta_n)] \tag{7}$$

where $2\theta_n$ is the conduction angle for each function, F_n, which, for an RF amplitude, A, and an input bias V_{GG}, can be computed as

$$2\theta_n = \mathrm{real}\left(2\mathrm{acos}\left(-\frac{V_{\mathrm{GG}} - b_n}{A}\right)\right). \tag{8}$$

Please note that I_0 and I_1 represent the dc and fundamental components of a current waveform that tends to a square wave as the PA is driven deeper into saturation. This waveform is significantly different from the one observed in overdriven class-B PAs, where the short circuit harmonic terminations ensure that the drain voltage is always sinusoidal. This imposes a limit on the amplitude of the fundamental drain voltage component, $V_{1\_\max} = V_{\mathrm{DD}} - V_K$, and, consequently, I_1 also becomes limited at

$$I_{1\_\max} = \frac{V_{\mathrm{DD}} - V_K}{R_L}. \tag{9}$$

However, if the current waveform is allowed to be square, the fundamental current component can indeed surpass this limit, as predicted by the model, and normally observed in class-F^{-1} PAs.

We start by analyzing how both V_{GG} and A impact the Fourier components (6) and (7), assuming that $K_2 = -K_1$, for different classes of operation. The bias voltages for each class are computed as $V_{\mathrm{GG}} = V_T + h \cdot I_{\max}/K_1$, with

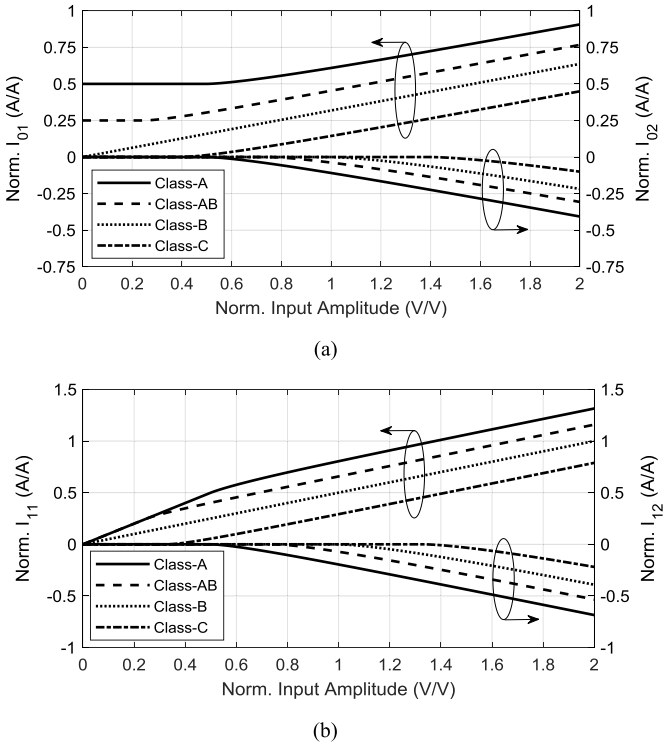

Fig. 5. Model predicted (a) dc and (b) fundamental components of each i_{DS} term, biased at different classes of operation, and normalized to $I_{\max}$. The input amplitude is normalized to $b_2 - b_1 = I_{\max}/K_1$.

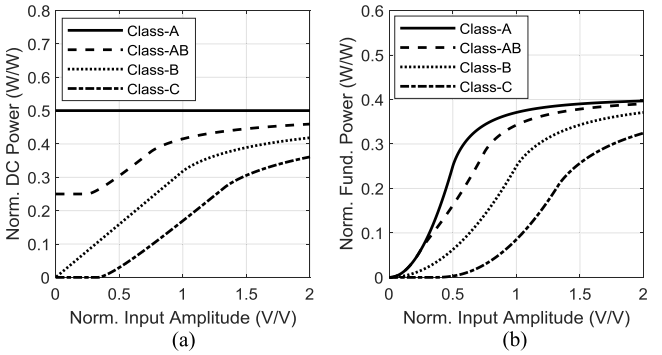

Fig. 6. Model predicted (a) dc and (b) fundamental powers, normalized to $I_{\max} V_{\mathrm{DD}}$, for a piecewise linear current source biased at different classes of operation.

$h = \{0.5, 0.2, 0, -0.3\}$, corresponding to classes-A, AB, B, and C, respectively. The dc and fundamental components of i_{DS}, I_0, and I_1, respectively, are presented in Fig. 5, normalized to $I_{\max}$. Note that each component is the sum of two terms as described in (6) and (7), one for each basis function of the model, denoted by the index n. The combination of these terms ($I_0 = I_{0,1} + I_{0,2}$ and $I_1 = I_{1,1} + I_{1,2}$) leads to the dc and output powers and efficiency profiles presented in Figs. 6 and 7, respectively. The class-A bias voltage is defined as the sum of the threshold voltage, V_T, with half of the voltage excursion, $0.5\, I_{\max}/K_1$, with K_1 representing the device transconductance G_m, the class-B is defined with a bias voltage equal to V_T, and the class-AB is with a bias voltage in-between class-A and class-B. Class-C is defined with a bias below V_T voltage.

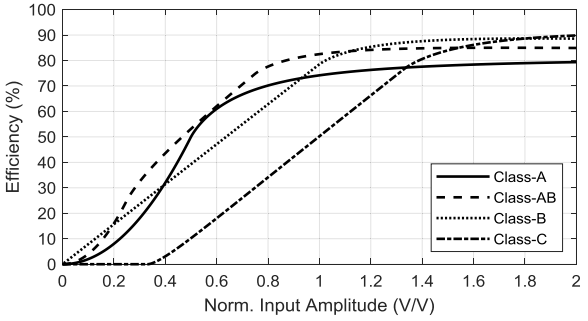

Fig. 7. Model predicted efficiency for a piecewise current source biased at different classes of operation. The input amplitude is normalized to $b_2 - b_1 = I_{\max}/K_1$.

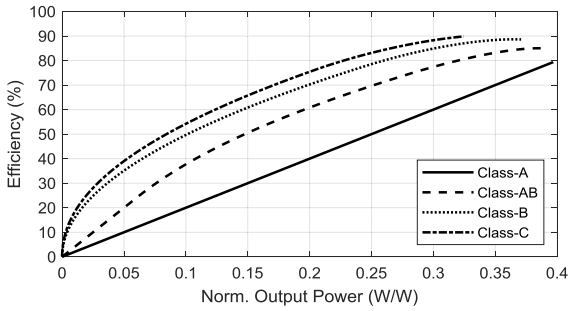

Fig. 8. Efficiency versus output power normalized to $I_{\max} V_{\mathrm{DD}}$, predicted by the model, for a piecewise current source biased at different operation classes.

The first observation we can make from the analysis of these results is that the second i_{DS} terms ($I_{0,2}$ and $I_{1,2}$) are only excited for very large-input power level in the same manner for all operation classes, as observed in Fig. 5. Since these terms represent the PA's compression, they only start to have an impact earlier or later, depending on the PA gain. Until there, the efficiency is mostly governed by the first i_{DS} terms ($I_{0,1}$ and $I_{1,1}$), the ones that describe the current mode operation.

Another aspect that we would like to highlight is the efficiency profile of the class-AB in comparison with the class-B PA. Looking into Fig. 7, it is possible to conclude that, for some input power levels, the efficiency of a class-AB PA is higher. This could be unexpected as we normally think in terms of the maximum efficiency (considering the onset of PA saturation) and that the PA is terminated with the optimum impedance for each operation class. However, this can be easily understood since an ideal class-B PA can have a maximum efficiency of $\pi/4$ and, therefore, at half of its input voltage excursion, its efficiency will be $\pi/8$, whereas, due to the higher gain of the class-A PA, this one will reach the maximum efficiency of 0.5, which is higher. Thus, if we sweep the input power, we start to see almost no efficiency in a class-AB PA, due to the large dc component without any output power, and then, due to the higher gain, the efficiency will grow faster.

In fact, if we represent the efficiency versus output power, as shown in Fig. 8, the class-B efficiency is always higher than the class-AB efficiency for the same output power level. However, representing the performance versus input power

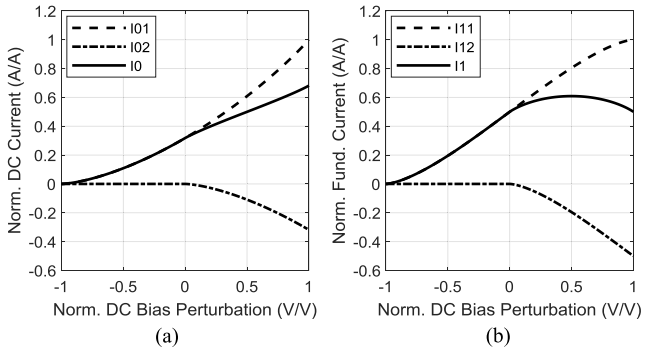

Fig. 9. Model predicted (a) dc current components and (b) fundamental current components normalized to the maximum current of the device, $I_{\max}$. The dc bias perturbation is normalized to $b_2 - b_1 = I_{\max}/K_1$.

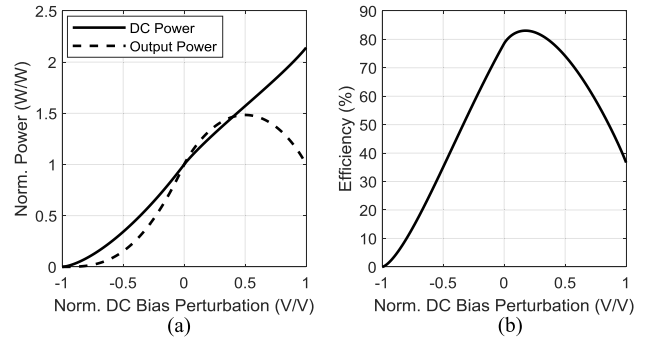

Fig. 10. Model predicted (a) dc and output powers normalized to the respective dc and fundamental powers obtained for a class-B at the onset of saturation and (b) the efficiency for swept dc bias voltage and under CW excitation at the edge of current saturation for class-B bias. The dc bias perturbation is normalized to $b_2 - b_1 = I_{\max}/K_1$.

will be helpful to understand the efficiency degradation, due to the input baseband voltage fluctuation, when the envelope amplitude and the baseband voltage are changing in time.

Then, we evaluated the PA's performance with respect to the input bias voltage for fixed excitation amplitude (which will correspond to the baseband voltage variations when a modulated signal will be used). Thus, considering optimal load impedance and constant CW excitation with maximum amplitude for a class-B PA, the obtained dc and fundamental current components for different input bias voltages (normalized to the threshold voltage, i.e., the nominal bias of a class-B PA) are presented in Fig. 9.

When the bias voltage is reduced below the nominal bias, the peak voltage of the signal is lower due to the fixed amplitude excitation, meaning that $I_{0,1}$ and $I_{1,1}$ are the only components that are excited, and both components decrease as the PA is biased deeper into class-C. Thus, since the output power is quadratically dependent on I_1 and the dc power is approximately proportional to I_0, the efficiency decreases monotonically, as observed in Fig. 10. Please note that, to be easier to understand the change in the PA performance to the nominal bias ($V_{\rm GG} = V_T$) we normalized the obtained powers to the ones calculated for the nominal bias, meaning that, for $V_{\rm GG} = V_T$, both powers are equal to one.

Conversely, when the bias voltage is increased from the class-B bias voltage, the second terms $I_{0,2}$ and $I_{1,2}$ become progressively higher due to the current waveform clipping. Both the total dc and fundamental currents decrease with respect to the case where only the components $I_{0,1}$ and $I_{1,1}$ are considered, reducing the fundamental component, the output power, and the efficiency. However, there is a zone where if we increase the bias $V_{\rm GG}$ into class-AB, these components increase more slowly than $I_{0,1}$ and $I_{1,1}$, and the efficiency increases slightly due to the higher fundamental component of class-AB operation. Consequently, it is expected that the efficiency slightly increases for a small increase of $V_{\rm GG}$, but for higher changes of $V_{\rm GG}$, the efficiency will drop.

To study the impact of the baseband fluctuation on the PA's performance, we used two-tone signals with a fixed peak amplitude. For narrowband operation, when the baseband frequency spectral lines do not overlap with the fundamental components, i.e., for the case where the two-tone frequency separation, $2\omega_m$, is much smaller than the carrier frequency, ω_c, the envelope amplitude can be interpreted as a change of the amplitude A in (6) and (7), whereas the baseband voltage fluctuation can be interpreted as a bias variation, $V_{\rm GG}$.

As described in Section II, the amplitude modulation of the signal generates a baseband current in the nonlinear $C_{\rm GS}$ capacitance, as derived in (4). Since the nonlinear $C_{\rm GS}$ is modeled through a first-order polynomial, and we are assuming that the fundamental components are a pure two-tone excitation, the baseband current can only have one frequency component at the two-tone frequency separation, $2\omega_m$. This current is supplied through a nonzero complex bias impedance, $Z_{S\_\rm BB}$, and produces a sinusoidal bias voltage fluctuation at the intrinsic gate terminal. Distinct performance degradation patterns are generated depending on the amplitude and phase of $Z_{S\_\rm BB}$, that we explore in detail in Sections III-A–III-C.

A. Inductive Input Baseband Impedance

First, we consider the scenario where $Z_{S\_\rm BB}(2\omega_m)$ is purely inductive, i.e., the situation that usually happens when PAs are excited with modulated signals whose bandwidth is below the input bias network parallel resonance frequency. From (5), it is observed that $v_{\rm bb}(t)$ is delayed by 90° with respect to $i_{\rm bb}(t)$ and, as this current is 90° in advance to the RF envelope voltage, the sinusoidal baseband voltage is added in-phase to the envelope of the two-tone signal, i.e., the minimum and maximum of both baseband and envelope amplitude occur at the same time. Fig. 11(a) presents the obtained bias fluctuation for three values of $|Z_{S_{\rm BB}}|$ (which corresponds to an impedance, that is 0×, 25×, and 50× higher than the fundamental impedance), i.e., three different inductances. Please note that we have included the short circuit to mimic the ideal class-B case.

For an intermediate amplitude level of baseband impedance, $Z_{S\_\rm BB2}$, in the low power region, the dc bias point becomes lower than the threshold voltage, imposing a class-C operation (or even cut-off at very low envelope amplitude). Therefore, in this region, the efficiency is degraded. Conversely, in the high-power region, the bias voltage increases and, thus, the PA

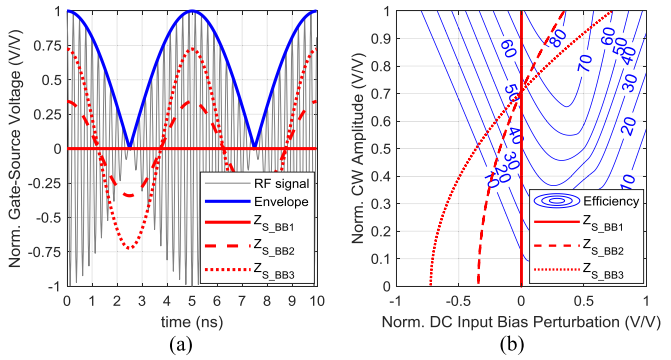

Fig. 11. Model predicted (a) envelope of the two-tone signal and (b) efficiency contours, where the dynamic bias fluctuation for three different purely inductive baseband impedances are overlapped. The dc bias perturbation and the gate-to-source voltage are both normalized to $b_2 - b_1 = I_{\max}/K_1$.

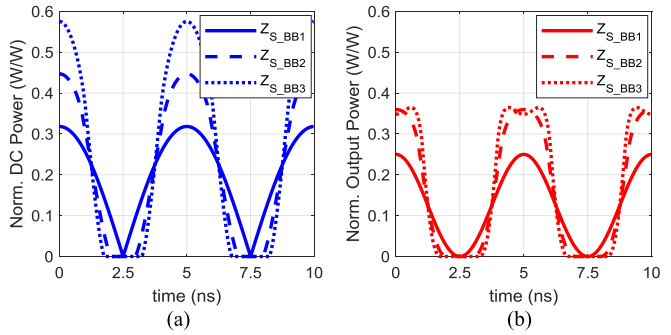

Fig. 12. Model predicted (a) dc power and (b) fundamental power waveforms normalized to $I_{\max} V_{DD}$ for three different purely inductive baseband impedances.

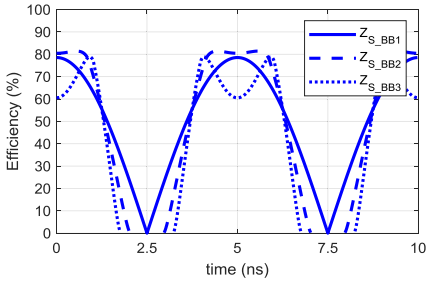

	Avg. Eff. (%)
Z_{S_BB1}	61.7
Z_{S_BB2}	72.4
Z_{S_BB3}	66.2

Fig. 13. Model predicted instantaneous efficiency waveform for three different purely inductive baseband impedances and the respective average efficiency computed from the average dc and output powers.

becomes biased at class-AB. However, since the excitation amplitude is fixed, the peak voltage also increases, reaching the region where the instantaneous current starts to saturate, i.e., where the second i_{DS} piecewise linear branch starts to have an impact. At the intermediate power region, the bias fluctuation is very small, and therefore, the PA operates with the nominal class-B bias, showing nearly the same performance.

This variation of operation classes is in accordance with what was observed in the instantaneous dc and fundamental power waveforms, presented in Fig. 12, and in the respective instantaneous efficiency presented in Fig. 13.

For the selected Z_{S_BB2}, the second term of i_{DS} is not severely excited and, therefore, according to what was previously presented, the instantaneous efficiency is higher in the high-power region due to the class-AB bias, and lower at

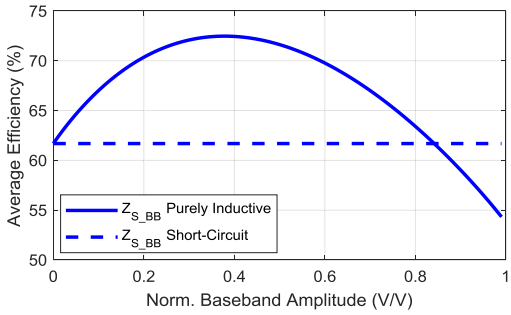

Fig. 14. Model predicted two-tone average efficiency at several bias fluctuation amplitudes for a purely inductive bias impedance. The baseband amplitude is normalized to the peak amplitude of the two-tone signal, $b_2 - b_1 = I_{\max}/K_1$.

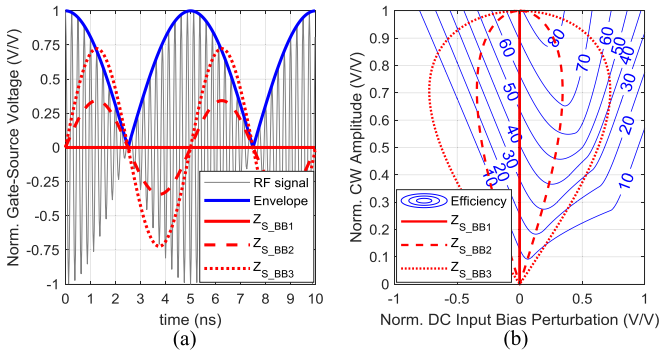

Fig. 15. Model predicted (a) envelope of the two-tone signal and (b) efficiency contours, where the dynamic bias fluctuation for three different purely resistive baseband impedances are overlapped. The dc bias perturbation and the gate-to-source voltage are both normalized to $b_2 - b_1 = I_{\max}/K_1$.

the low power region due to class-C operation with the same excitation amplitude. The instantaneous dc and output powers at the envelope high-power region will have more impact on the PA performance, since the PA will operate more time in this region according to the probability density function (PDF) of the two-tone signal envelope amplitude, being expected a higher average efficiency.

However, note that if the fluctuation is very high, i.e., higher baseband impedance, as it is the case of Z_{S_BB3}, or two-tone frequency separation, the PA becomes biased closer to class-A at the high-power region of the envelope and, therefore, the second term of i_{DS} becomes dominant, which results in an efficiency decrease. This can be observed in Fig. 14, where the bias fluctuation was swept.

Please note that, if the magnitude of $Z_{S\_BB}(2\omega_m)$ is sufficiently high, the baseband amplitude fluctuation can be so large that it biases the PA at class-A in the high-power region and at deep class-C in the low-power region. Therefore, the transistor's absolute maximum ratings may be crossed, permanently damaging the device.

B. Resistive Input Baseband Impedance (Resonance)

When $Z_{S\_BB}(2\omega_m)$ is purely resistive, e.g., when the input bias circuit reaches its parallel resonance, the baseband component and the RF envelope are in quadrature, following (5), and as shown in Fig. 15 for three different magnitudes of $Z_{S\_BB}(2\omega_m)$, which corresponds to an impedance that is $0\times$, $25\times$, and $50\times$ higher than the fundamental impedance.

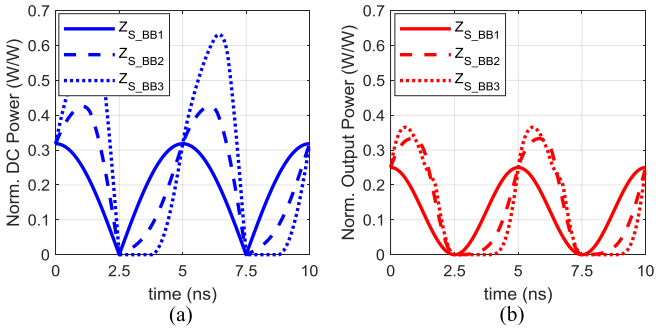

Fig. 16. Model predicted (a) dc power and (b) fundamental power waveforms normalized to $I_{\max} V_{DD}$ for three different purely resistive baseband impedances.

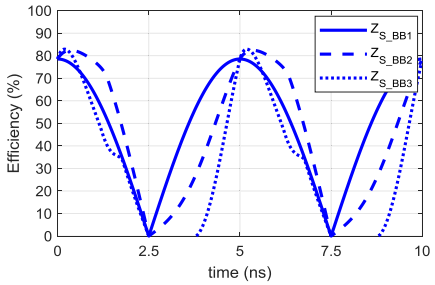

	Avg. Eff. (%)
Z_{S_BB1}	61.7
Z_{S_BB2}	64.5
Z_{S_BB3}	50.6

Fig. 17. Model predicted instantaneous efficiency waveform for three different purely resistive baseband impedances and the respective average efficiency computed from the average dc and output powers.

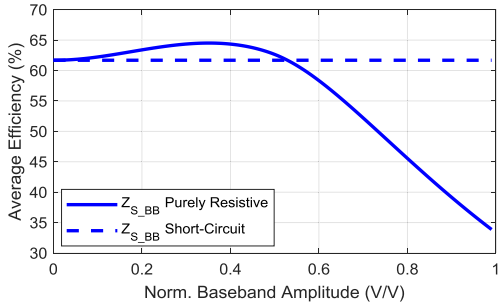

Fig. 18. Model predicted two-tone average efficiency at several bias fluctuation amplitudes for a purely resistive bias impedance. The baseband amplitude is normalized to the peak amplitude of the two-tone signal, $b_2 - b_1 = I_{\max}/K_1$.

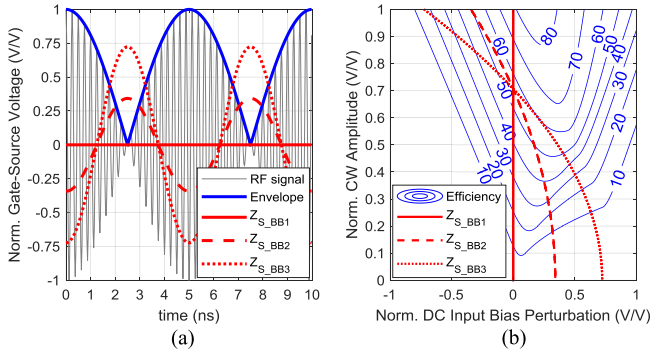

Fig. 19. Model predicted (a) envelope of the two-tone signal and (b) efficiency contours, where the dynamic bias fluctuation for three different purely capacitive baseband impedances are overlapped. The dc bias perturbation and the gate-to-source voltage are both normalized to $b_2 - b_1 = I_{\max}/K_1$.

If $Z_{S\_BB}(2\omega_m)$ is purely resistive, the obtained bias fluctuation is zero at both the high- and very low-power regions of the envelope. However, the maximum negative and positive bias fluctuations occur at mid-power levels on the ascending and descending envelope regions, respectively.

Thus, when the bias fluctuation is small (i.e., when the first term of the i_{DS} is dominant, as is the case of Z_{S_BB2}), an efficiency degradation is observed in the ascending envelope due to the class-C operation, but it is compensated by a similar efficiency increase in the descending envelope region, where it operates at class-AB.

Since the dc and output power curves are not purely symmetric with respect to the input bias, leading to the asymmetric efficiency contours presented in Fig. 15 (b), a slight increase in the average efficiency is expected for low baseband impedance. The waveforms of the instantaneous dc and output power and the respective efficiency are presented in Figs. 16 and 17, respectively.

However, if the bias fluctuation is sufficiently high (e.g., as is the case of Z_{S_BB3}), the PA becomes biased near class-A during part of the descending envelope where the $I_{1,2}$ term becomes dominant, and the efficiency decreases due to the lower output power, as we have seen previously in Fig. 10. Since the instantaneous efficiency now also degrades in the descending envelope, it is expected that the average efficiency decreases.

To observe this efficiency behavior, Fig. 18 presents the computed average efficiency as the baseband fluctuation is swept. As expected, for low amplitude bias fluctuation, the average efficiency is unaffected and starts to degrade as the amplitude increases.

C. Capacitive Input Baseband Impedance

Finally, when $2\omega_m$ is already above the parallel resonant frequency, so that the baseband impedance at the envelope frequency $Z_{S\_BB}(2\omega_m)$ is purely capacitive, the RF envelope and the baseband voltage are in the opposite phase, according to (5), and as presented in Fig. 19 (again for three different magnitude values of $Z_{S\_BB}(2\omega_m)$, which corresponds to an impedance that is $0\times$, $25\times$, and $50\times$ higher than the fundamental impedance). Thus, the baseband fluctuation is at its minimum when the envelope is at the maximum amplitude and, conversely, at its maximum when the envelope amplitude is lowest.

Therefore, the PA operates at class-A with lower efficiency in the very low-power region of the envelope, and at class-C in the high-power region, where the efficiency is also lower due to the constant excitation amplitude. However, at the medium–low-power region, the efficiency is higher because the PA becomes biased at class-AB. This is what is shown in Figs. 20 and 21, for the dc and fundamental powers and efficiency, respectively.

Nevertheless, for a two-tone signal, the efficiency at the highest power region has the most impact on the average efficiency due to the PDF's profile. Therefore, we should always observe efficiency degradation in this scenario,

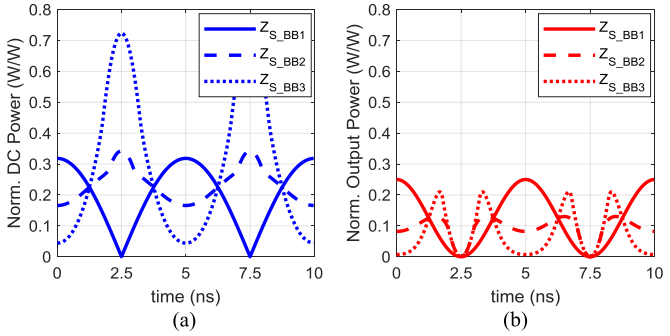

Fig. 20. Model predicted (a) dc power and (b) fundamental power waveforms normalized to $I_{\max} V_{DD}$ for three different purely capacitive baseband impedances.

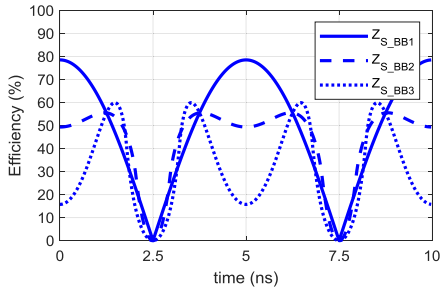

	Avg. Eff. (%)
Z_{S_BB1}	61.7
Z_{S_BB2}	39.6
Z_{S_BB3}	25.4

Fig. 21. Model predicted instantaneous efficiency waveform for three different purely capacitive baseband impedances and the respective average efficiency computed from the average dc and output powers.

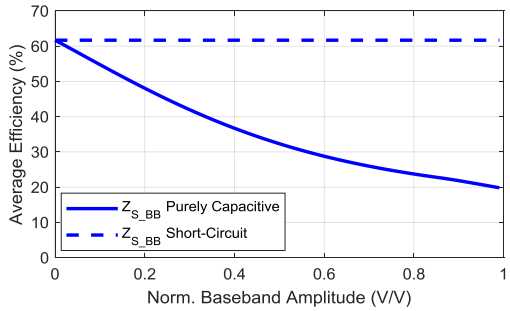

Fig. 22. Model predicted two-tone average efficiency at several bias fluctuation amplitudes and for a purely capacitive bias impedance. The baseband amplitude is normalized to the peak amplitude of the two-tone signal, $b_2 - b_1 = I_{\max}/K_1$.

regardless of the baseband fluctuation's amplitude. This is, indeed, the observed efficiency profile presented in Fig. 22, in which the baseband voltage amplitude is swept.

IV. Experimental Results

In order to quantitatively evaluate the efficiency and linearity degradation expected in a real device, two PAs with different input bias networks were designed using Wolfspeed's CGH27030F GaN HEMT and implemented on a 0.76-mm Isola Astra substrate. A photograph of the implemented PAs is presented in Fig. 23 and the circuit IMNs representations for PA1 and PA2 and their OMN are presented in Figs. 24 and 25, respectively.

The IMN and OMN were designed to minimize the variation of the efficiency, output power, and gain profiles over a 650-MHz bandwidth span. The simulated and measured

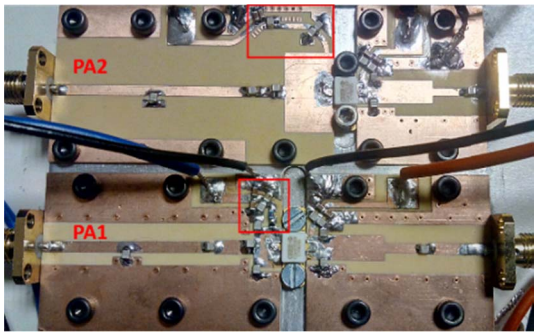

Fig. 23. Photograph of the implemented PAs.

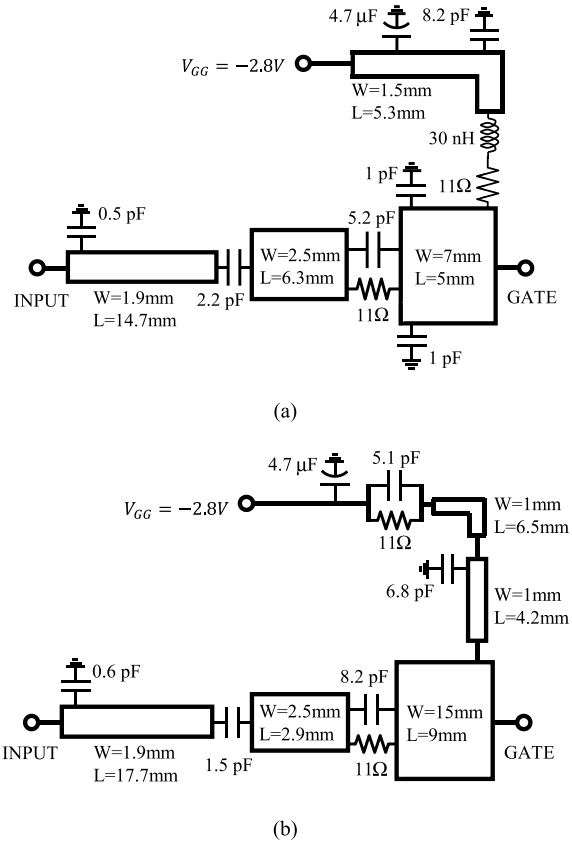

Fig. 24. IMN of (a) PA1 and (b) PA2.

efficiency, PAE, and output power of each PA, at the 2.5-dB compression level, are presented in Figs. 26 and 27, respectively.

While the OMN was optimally designed to obtain very low baseband impedance up to 1 GHz, the IMN of each PA was designed to present two distinct Z_{S_BB} profiles to evaluate efficiency and linearity degradation. One was conceived to correspond to the conventional structure previously presented in Fig. 2(a) (PA1), while another was appropriately designed to avoid a parallel resonance with the device's input impedance (PA2). This was achieved by adding a capacitor in parallel with the low-frequency stabilization resistor and by replacing the inductor by a short-length transmission line. In practice, this is the same as reducing the quality factor of the parallel resonant circuit and increasing the resonance frequency. With these changes, the input matching for the fundamental and the

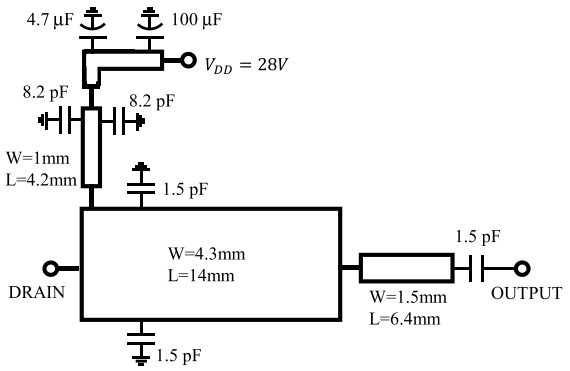

Fig. 25. OMN of the implemented PAs.

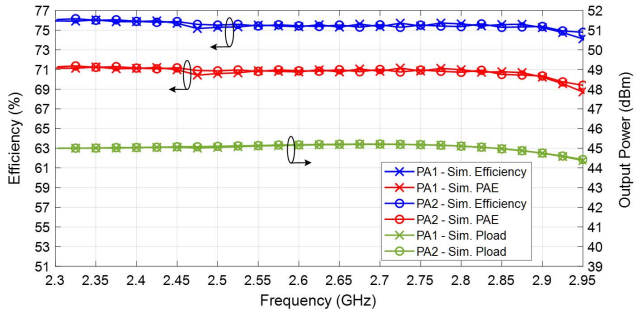

Fig. 26. Simulated efficiency, PAE, and output power under CW excitation, at the 2.5-dB gain compression point.

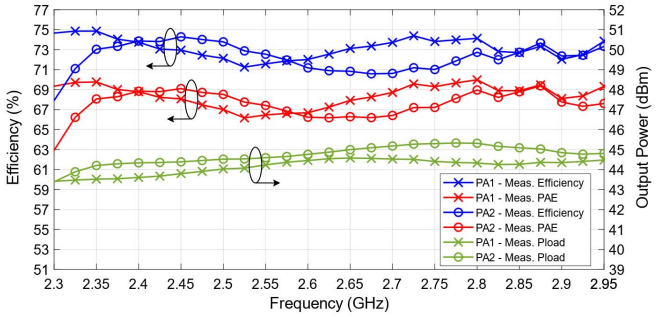

Fig. 27. Measured efficiency, PAE, and output power under CW excitation, at the 2.5-dB gain compression point.

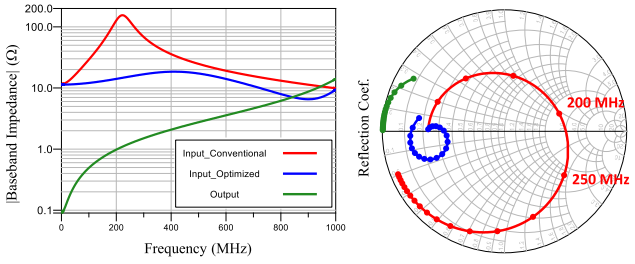

Fig. 28. Simulated baseband impedance profiles at the intrinsic gate and drain reference planes for the designed input and output networks.

bias circuit must be designed together since, without the large inductor, they will load one another. Both impedance profiles are presented in Fig. 28.

The dynamic behavior of the PA was assessed under a two-tone excitation, centered at 2.55 GHz, with a constant average available power of 26 dBm. The separation between the tones was swept between 10 and 400 MHz. The simulated and

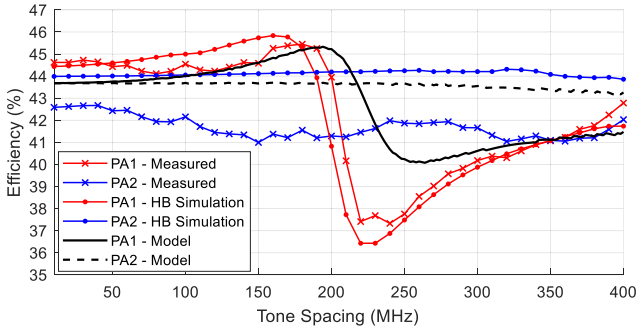

Fig. 29. Simulated, measured, and model predicted the average efficiency of both implemented PAs, under two-tone excitation.

TABLE I
MODEL PARAMETERS

Name	Value
K_1	1.23 S
b_1	-2.8 V
K_2	-0.98 S
b_2	-0.5 V
C_{gs0}	12.1 pF
C_{gs1}	1.27 pF/V

measured average efficiency is presented in Fig. 29, as reported in [13].

For PA1, both the simulated and measured average efficiencies have a sharp degradation of nearly 8% immediately above 200 MHz, where the impedance presented by the IMN at the baseband is closer to the parallel resonance. This is also the frequency region where the linearity of the PA is most degraded with an increase in the third-order IMD power of 15 dB, with respect to the initial tone separation of 10 MHz, as presented in the conference article [13].

Conversely, for the optimized network of PA2, both the efficiency and linearity remain nearly unchanged over the entire video bandwidth. The measured average efficiency is 2% lower at the lower tone separations and has higher variation over the instantaneous bandwidth than the one predicted by the simulation, which is attributed to the small differences in the CW figures of merit of each PA.

The theoretical model was validated by comparing the average efficiency behavior with the measurements as the tone separation increases. First, the model's parameters (K_n, b_n, and C_{GS} parameters) were fit to reproduce the performance of the implemented PAs under CW excitation, see Table I. Then, we computed the average efficiency for the same tone separation sweep and input available power that we used in the measurements. The computed average efficiency is presented in Fig. 29. The model is able to predict the qualitative behavior by presenting the same profile over the full frequency separation sweep.

The model also predicts the efficiency within a 2% tolerance, except in the 200–250-MHz tone separation range where the baseband impedance is very high and the first-order approximation of the C_{GS} capacitance is insufficient. In addition, since the model is built under the assumption that the RF envelope is independent of the generated baseband

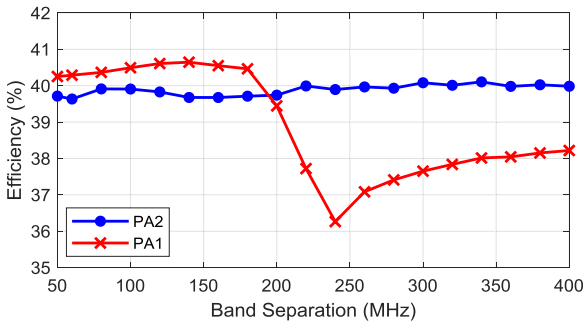

Fig. 30. Measured average efficiency of each implemented PA under concurrent dual-band LTE signals, with 5-MHz bandwidth, for several band separations.

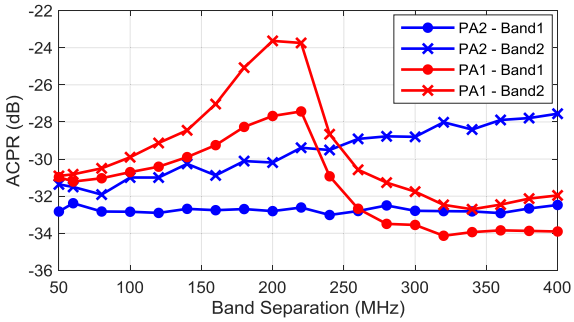

Fig. 31. Measured ACPR of each implemented PA under concurrent dual-band LTE signals, with 5-MHz bandwidth, for several band separations.

distortion, this inaccuracy cannot be fully removed without using a recursive algorithm to accurately determine the intrinsic v_{GS} voltage.

Nevertheless, the frequency at which the efficiency degradation is maximum is predicted with an error of about 25 MHz that is usually enough for most PA applications where designers are interested in evaluating the instantaneous bandwidth.

Finally, we tested each PA in concurrent dual-band operation with 5-MHz orthogonal frequency-division multiplexing (OFDM) signals at each band with a peak-to-average power ratio (PAPR) of 9.7 dB. The separation between bands was swept from 50 to 400 MHz at a center frequency of 2.55 GHz. Power equalization was performed at the output, in single-band operation, to ensure that the PA is driven up to the same output peak power level in both bands and for all band separation values. The selected output power level was the one that would lead to a similar gain compression of 2.5 dB for each PA presented in Fig. 27.

First, the PA was driven at each band independently, i.e., in single-band operation, and the output signal was linearized using digital pre-distortion (DPD), obtaining in this way the desired reference condition and output peak power level. Then, both bands were driven simultaneously to measure the adjacent channel power ratio (ACPR) at each band and the average efficiency. Although the power equalization could be done by simply increasing the power of the input signal of each band, the benefit of DPD is that, conceptually, if the PA behaved linearly in the presence of both bands, the output signal would be undistorted. Therefore, the distortion that we now measure is a direct consequence of driving the PA with a wide concurrent band signal due to cross modulation.

The efficiency variation profile in PA1, presented in Fig. 30, closely follows the one predicted by the model and observed in the measurements with two-tone signals, as previously shown in Fig. 27. In addition, a clear degradation of the PA's linearity near the 200-MHz band separation is observed in the measured ACPR, which is presented in Fig. 31. This result complements the IMD3 measurements that were performed in [13], by showing that even if one could filter out the out-of-band IMD components at the output, the improper input baseband profile also generates in-band distortion that can only be removed with DPD.

In PA2, both the average efficiency and ACPR profiles are nearly flat near the 200-MHz band separation, which indicates that the cause of the observed degradation was eliminated.

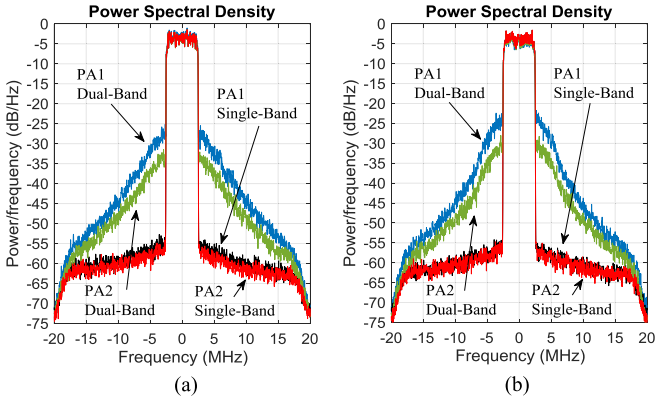

Fig. 32. Measured normalized output spectrum of the (a) left and (b) right fundamental bands, at an output peak power of 44.5 dBm, under single- and dual-band LTE excitations, with DPD, extracted for single-band operation.

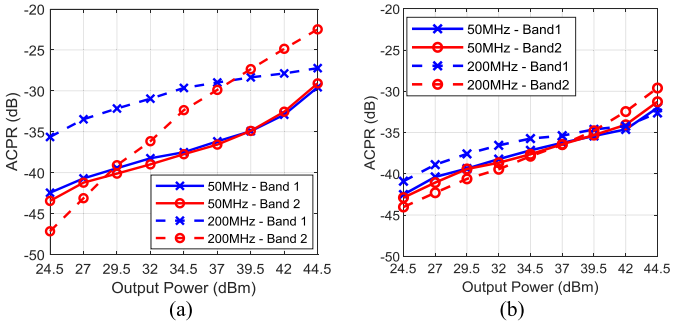

Fig. 33. ACPR of (a) PA1 and (b) PA2, when operated in concurrent dual-band excitation, measured for several output peak power levels at each band calibrated in single-band operation using DPD.

These results indicate that the efficiency degradation behavior predicted for two-tone signals is closely correlated with the one observed with real dual-band communication signals. The ability to roughly predict the efficiency degradation profile with a simple and analytic model is not only a significant improvement to the overall design process but also provides insight on the underlying degradation mechanisms that can be useful for higher complexity PAs.

The output spectra of both long-term evolution (LTE) bands, for the 200-MHz frequency spacing and at a peak output power of 44.5 dBm, are presented in Fig. 32. As observed, with the DPD correction performed for each band individually, we decreased the ACPR to -50 dBc at the desired output power level. Then, under concurrent band operation, the increase of distortion in PA1 is higher than the one observed for PA2.

Finally, the linearity degradation versus output power for the 50- and 200-MHz frequency separations is presented in Fig. 33. Naturally, both PAs present similar distortion behavior when the frequency separation is small. However, for the 200-MHz separation, a clear increase of the ACPR in PA1 is observed, even at low-power levels, whereas in the PA2, the ACPR profile is practically unchanged.

V. Conclusion

This article relates the limited PA efficiency performance observed in certain circumstances with the input network baseband terminations. The source of this limitation lies on the parallel network composed by the IMN baseband impedance termination and the device input capacitance, producing a large intrinsic gate voltage modulation at baseband frequencies. The corresponding PA conduction angle modulation leads to a degradation of both the linearity and efficiency. A simple theoretical model that predicts the qualitative efficiency variation profile of the PA under concurrent band operation was presented. We demonstrated that the model provides not only a qualitative understanding of the degradation mechanism but also an estimation of the input baseband impedance impact on the PA's performance.

This degradation mechanism was experimentally verified and demonstrates that if the IMN baseband impedances are not properly chosen, the PA can present an average efficiency much lower than the one obtained from the expected theoretical difference between the modulated and CW signals.

Acknowledgment

The authors would like to thank the PA Design Team—namely, Dr. F. Purroy—Huawei Technologies Sweden AB, Kista, Sweden, for interesting technical discussions regarding some of the observations dealt with within this article.

References

[1] X. Chen, W. Chen, G. Su, F. M. Ghannouchi, and Z. Feng, "A concurrent dual-band 1.9–2.6-GHz Doherty power amplifier with Intermodulation impedance tuning," in *IEEE MTT-S Int. Microw. Symp. Dig.*, Tampa, FL, USA, Jun. 2014, pp. 1–4.

[2] X. Chen, W. Chen, F. M. Ghannouchi, Z. Feng, and Y. Liu, "Enhanced analysis and design method of concurrent dual-band power amplifiers with intermodulation impedance tuning," *IEEE Trans. Microw. Theory Techn.*, vol. 61, no. 12, pp. 4544–4558, Dec. 2013.

[3] J. Li, W. Chen, F. Huang, and Z. Fend, "Multiband and multimode concurrent PA with novel intermodulation tuning network for linearity improvement," *IEEE Microw. Wireless Compon. Lett.*, vol. 28, no. 3, pp. 248–250, Mar. 2018.

[4] D. J. Williams, J. Leckey, and P. J. Tasker, "Envelope domain analysis of measured time domain voltage and current waveforms provide for improved understanding of factors effecting linearity," in *IEEE MTT-S Int. Microw. Symp. Dig.*, Philadelphia, PA, USA, vol. 2, Jun. 2003, pp. 1411–1414.

[5] B. Bunz, A. Ahmed, and G. Kompa, "Influence of envelope impedance termination on RF behaviour of GaN HEMT power devices," in *Proc. Eur. Gallium Arsenide Other Semiconductor Appl. Symp. (GAAS)*, Paris, France, Oct. 2005, pp. 649–652.

[6] Y. Hu, J. C. Mollier, and J. Obregon, "A Nevv method of third-order intermodulation reduction in nonlinear microwave systems," *IEEE Trans. Microw. Theory Techn.*, vol. MTT-34, no. 2, pp. 245–250, Feb. 1986.

[7] Y.-P. Kwon, Y.-C. Jeong, Y. Kim, and C.-D. Kim, "A design of predistortion linearizer using 2nd order low frequency intermodulation signal injection," in *Proc. IEEE 33rd Eur. Microw. Conf.*, Munich, Germany, Oct. 2003, pp. 249–252.

[8] M. Akmal, "Broadband baseband impedance control for linearity enhancement in microwave devices," *Int. J. Elect., Comput., Energetic, Electron. Commun. Eng.*, vol. 9, no. 8, pp. 953–959, Dec. 2015.

[9] I. Takenaka, K. Ishikura, H. Takahashi, K. Hasegawa, K. Asano, and N. Iwata, "Improvement of intermodulation distortion asymmetry characteristics with wideband microwave signals in high power amplifiers," *IEEE Trans. Microw. Theory Techn.*, vol. 56, no. 6, pp. 1355–1363, Jun. 2008.

[10] M. J. Pelk, L. C. N. de Vreede, M. Spirito, and J. H. Jos, "Base-band impedance control and calibration for on-wafer linearity measurements," in *Proc. ARFTG 63rd Conf. Spring*, Fort Worth, TX, USA, 2004, pp. 35–40.

[11] M. Akmal *et al.*, "The effect of baseband impedance termination on the linearity of GaN HEMTs," in *Proc. IEEE 40th Eur. Microw. Conf.*, Paris, France, Sep. 2010, pp. 1046–1049.

[12] L. C. Nunes, D. R. Barros, P. M. Cabral, and J. C. Pedro, "Efficiency degradation analysis in wideband power amplifiers," *IEEE Trans. Microw. Theory Techn.*, vol. 66, no. 12, pp. 5640–5651, Dec. 2018.

[13] D. R. Barros, L. C. Nunes, P. M. Cabral, and J. C. Pedro, "Impact of the input baseband impedance on the instantaneous bandwidth of wideband power amplifiers," in *IEEE MTT-S Int. Microw. Symp. Dig.*, Boston, MA, USA, Jun. 2019, pp. 1–4.

[14] L. C. Nunes, P. M. Cabral, and J. C. Pedro, "AM/AM and AM/PM distortion generation mechanisms in Si LDMOS and GaN HEMT based RF power amplifiers," *IEEE Trans. Microw. Theory Techn.*, vol. 62, no. 4, pp. 799–809, Apr. 2008.

[15] C. Fager, J. C. Pedro, N. B. de Carvalho, H. Zirath, F. Fortes, and M. J. Rosario, "A comprehensive analysis of IMD behavior in RF CMOS power amplifiers," *IEEE J. Solid-State Circuits*, vol. 39, no. 1, pp. 24–34, Jan. 2004.

[16] J. C. Pedro, L. C. Nunes, and P. M. Lavrador, "A new large-signal intermodulation and spurious analysis tool," in *IEEE MTT-S Int. Microw. Symp. Dig.*, Seattle, WA, USA, Jun. 2013, pp. 1–4.

Diogo R. Barros (S'14) was born in Penalva do Castelo, Portugal, in 1990. He received the M.Sc. degree in electronics and telecommunications engineering from the University of Aveiro, Aveiro, Portugal, in 2015, where he is currently pursuing the Ph.D. degree in electrical engineering.

He has been a Junior Researcher with the Institute of Telecommunications, Aveiro, since 2016. His current research interests include nonlinear distortion analysis, wideband high-efficiency PA design, and advanced MISO Doherty-outphasing power amplifier architectures.

Mr. Barros is a Student Member of the IEEE Microwave Theory and Techniques Society (IEEE MTT-S) and a member of the IEEE MTT-S Student Branch Chapter at the University of Aveiro.

Luís C. Nunes (S'13–M'17) was born in Guarda, Portugal, in 1986. He received the M.Sc. and Ph.D. degrees in electrical engineering from the University of Aveiro, Aveiro, Portugal, in 2010 and 2015, respectively.

From 2016 to 2017, he was an RF Design Engineer with Huawei Technologies Sweden AB, Kista, Sweden. He is currently a Researcher Assistant with the Institute of Telecommunications, Aveiro. His current research interests include active device modeling, nonlinear distortion analysis, and the design of microwave circuits, especially high-efficiency and linear power amplifiers.

Dr. Nunes is a member of the IEEE Microwave Theory and Techniques Society and the IEEE Electron Devices Society.

Pedro M. Cabral (S'04–M'07–SM'16) was born in Aveiro, Portugal, in 1979. He received the Electrical Engineering and the Ph.D. degrees from the University of Aveiro, Aveiro, Portugal, in 2002 and 2006, respectively.

He is currently a Senior Researcher with the Institute of Telecommunications, Aveiro, and an Assistant Professor with the University of Aveiro. His current research interests include active device nonlinear modeling, design of microwave circuits, high-efficiency power amplifiers, and wireless transmitter architectures.

Dr. Cabral has been a reviewer for several publications, including the IEEE TRANSACTIONS ON MICROWAVE THEORY AND TECHNIQUES, the IEEE TRANSACTIONS ON COMPUTER-AIDED DESIGN OF INTEGRATED CIRCUITS AND SYSTEMS, the IEEE TRANSACTIONS ON INSTRUMENTATION AND MEASUREMENT, and the IEEE TRANSACTIONS ON CIRCUITS AND SYSTEMS—I: REGULAR PAPERS.

José Carlos Pedro (S'90–M'95–SM'99–F'07) received the Diploma, Ph.D. and Habilitation degrees in electronics and telecommunications engineering from the University of Aveiro, Aveiro, Portugal, in 1985, 1993, and 2002, respectively.

He is currently a Full Professor with the University of Aveiro. His current research interests include active device modeling and the analysis and design of various nonlinear microwave circuits. He is the leading author of two books and has authored or coauthored more than 200 articles in international journals and symposia.

Prof. Pedro received various prizes, including the Marconi Young Scientist Award in 1993, the 2000 Institution of Electrical Engineers Measurement Prize, the 2015 EuMC Best Paper Microwave Prize, and the Microwave Distinguished Educator Award. He has served the scientific community by acting as a reviewer and editor of several conferences and journals, including the IEEE TRANSACTIONS ON MICROWAVE THEORY AND TECHNIQUES. He is currently the Editor-in-Chief of the IEEE TRANSACTIONS ON MICROWAVE THEORY AND TECHNIQUES.